



Microstructures and Properties of Graphite Nanoflake/6061Al Matrix Composites Fabricated via Spark Plasma Sintering

Guodong Chen, Hao Chang, Jian Sun, Bing Wang, Lei Yang, Jianhua Zhang, and Wenming Tang

(Submitted October 16, 2019; in revised form February 6, 2020; published online February 20, 2020)

Two types of graphite nanoflakes (GNFs), GNF_A for 30–100 μm in diameter and less than 100 nm in thickness, and GNF_B for 0.5–10 μm in diameter and less than 20 nm in thickness, were used to fabricate GNF/6061Al matrix composites with GNF fractions ranging from 5 to 15 wt.% via spark plasma sintering (SPS) at 610 °C under a load of 35 MPa. The effects of GNF size and content on microstructures and properties of the composites were investigated. The results show that uniform mixing of GNFs in the 6061Al powder was achieved through mechanical and ultrasonic stirring. When the GNFs were well dispersed, the composites were dense. An interfacial zone of 15–18 nm in thickness was formed and composed of two layers, a poorly crystalline layer and an amorphous layer. No Al_4C_3 was detected in the interfacial zone. The relative densities, bending strengths, thermal conductivities (TCs), and coefficients of thermal expansion (CTEs) (room temperature to 100 °C) of the 10 wt.% GNF_A /6061Al matrix composites were 98.5%, 120 MPa, 155 $\text{W m}^{-1} \text{K}^{-1}$ in the X – Y direction and 61 $\text{W m}^{-1} \text{K}^{-1}$ in the Z direction, and 14.2 ppm K^{-1} in the X – Y direction and 12.1 ppm K^{-1} in the Z direction, respectively. Those of the 10 wt.% GNF_B /6061Al matrix composites were 97.8%, 70 MPa, 110 $\text{W m}^{-1} \text{K}^{-1}$ in the X – Y direction and 90 $\text{W m}^{-1} \text{K}^{-1}$ in the Z direction, and 15.4 ppm K^{-1} in the X – Y direction and 14.7 ppm K^{-1} in the Z direction, respectively. The GNF_B /6061Al matrix composites showed lower differences of TC and CTE between the X – Y and Z directions. Therefore, the anisotropy of the microstructures and properties of the composites in three dimensions were significantly reduced.

Keywords graphite nanoflakes (GNFs), interface, mechanical property, metallic matrix composites, microstructure, powder metallurgy, thermal property

1. Introduction

Miniaturization and high-density packaging of microelectronics and power electronics bring new and notable challenges to electronic packaging materials (Ref 1–4). To solve this problem, carbon materials/Al matrix composites have been proposed, which have been shown to possess tremendous application potential in novel electronic packaging materials. Many carbon materials, such as natural graphite flakes, carbon nanotubes, carbon fibers, and graphene, have been successfully used as reinforcements to manufacture Al matrix electronic packaging composites of high thermal conductivities (TCs), low coefficients of thermal expansion (CTEs), and acceptable mechanical properties (Ref 5–10).

Generally, two-dimensional carbon materials among the above-mentioned carbon reinforcements, e.g., natural graphite flakes and graphene, are superior to one-dimensional carbon materials, such as carbon nanotubes and carbon fibers, in anisotropic reduction in the Al matrix composites, at least in the X – Y direction (parallel to the in-plane graphite flake). However, the anisotropy of Al matrix composites reinforced with large natural graphite flakes remains significant. For example, 50 vol.% natural graphite flakes/Al matrix composites synthesized via spark plasma sintering (SPS) show a low TC of 40 $\text{W m}^{-1} \text{K}^{-1}$ in the Z direction (perpendicular to the in-plane graphite flake), though it has an excellent TC in the X – Y direction (Ref 5). The uniform dispersion of graphene in the Al alloy matrix is still an insurmountable problem, although the uniform dispersion of a small amount of graphene (< 1 wt.%) in the Al alloy matrix seems possible using ultrasonic stirring (Ref 7). However, for the purposes of improving TC and reducing CTE of Al matrix electronic packaging composites significantly, higher loadings of graphene are required. In this situation, graphene aggregation in the composites is a difficult challenge, and, therefore, the performances of the composites are significantly reduced (Ref 11, 12). Accordingly, GNFs of a size between natural graphite flakes and graphene are expected to be more effective in improving the uniform distribution of the reinforcements, and thereby, reducing the anisotropy of the Al matrix composites (Ref 13).

C–Al is a binary reaction system where brittle, needle-like Al_4C_3 has been frequently reported as the interfacial reaction product in carbon materials/Al matrix composites fabricated via normal sintering and infiltration processes, which has a negative effect on the properties of the composites (Ref 9,

Guodong Chen, Hao Chang, Jian Sun, and Jianhua Zhang, School of Materials Science and Engineering, Hefei University of Technology, Hefei 230009, China; **Bing Wang and Lei Yang**, 43 Institute, China Electronics Technology Group Corporation, Hefei 230088, China; and **Wenming Tang**, School of Materials Science and Engineering, Hefei University of Technology, Hefei 230009, China; and National-Local Joint Engineering Research Center of Nonferrous Metals and Processing Technology, Hefei 230009, China. Contact e-mail: wmtang@hfut.edu.cn.

10, 14). SPS technology has many advantages including low sintering temperature, short holding time, and rapid heating and cooling rates (Ref 15, 16). It can be used to achieve rapid densification of GNF/Al matrix composites at low sintering temperatures, with the intent that the formation of Al_4C_3 can be effectively inhibited or even prevented, and further, the microstructures and properties of the composites are improved.

In the current study, two types of GNFs of different sizes, named GNF_A and GNF_B , were used as reinforcements to produce 6061Al matrix composites. The sizes of them are both at nanoscale, situated between those of the natural graphite flakes and graphene. The GNF amount is no more than 15 wt.%, ensuring enough strength and TC of the composites acting as electronic packaging materials. The GNFs were mixed with 6061Al powder via ultrasonic and mechanical stirring, and then, the GNF/6061Al powder mixtures were consolidated using the SPS technique. The effects of GNF size and content on the microstructures and mechanical and thermal properties of the GNF/6061Al matrix composites were investigated in detail. Moreover, the interfacial bonding characteristics of the GNF/6061Al matrix composites were also clarified. This work is believed to provide a useful reference for understanding the performance of graphite flakes/Al matrix composites.

2. Experimental Procedure

Nitrogen atomized 6061Al alloy powder, manufactured by Changsha Tianjiu Metal Co., Ltd., China, and two kinds of GNFs, provided by Q-CARBON Carbon Material Co., Ltd., China, were used as raw materials to prepare the GNF/6061Al matrix composites. As shown in Fig. 1(a) and (b), both GNF_A and GNF_B are nearly disk-like in shape. The edge of each GNF is slightly curled as a result of surface tension. GNF_A was 30–100 μm in diameter and less than 100 nm in thickness, and GNF_B was 0.5–10 μm in diameter and less than 20 nm in thickness. The purities of the GNFs were both more than 99%. The 6061Al powder has an average particle size (D_{50}) of 15 μm and an average chemical composition of 0.975 wt.% Mg, 0.59 wt.% Si, 0.092 wt.% Fe, 0.289 wt.% Cu, 0.08 wt.% Mn, 0.031 wt.% Zn, and Al the balance.

The GNFs were added at varying ratios of 5–15 wt.% to the 6061Al powder mixture and first dispersed in absolute ethanol and ultrasonically treated for 60 min using a KQ-50E-type ultrasonic disperser. After that, the 6061Al powder was placed into the GNFs–ethanol suspension. The suspension was then mechanically stirred for 8 h using a JJ-1-type precision

hydraulic stirrer, in tandem with ultrasonication. In the process of mechanical and ultrasonic stirring, a viscous slurry was gradually formed as ethanol volatilized. The slurry was then dried at 60 $^{\circ}\text{C}$ for 3 h in a GZX-9023MBE-type electrothermal blast drying box. Finally, the dried product was ground lightly in an agate mortar to obtain the GNFs and 6061Al powder mixture.

The powder mixture was filled into a graphite mold and isolated from the upper/lower pressure head of the graphite mold with graphite paper. The assembled graphite mold was placed in a LABOX-350-type discharge plasma sintering furnace. The sintering temperature, holding time, and axial load were fixed at 610 $^{\circ}\text{C}$, 10 min, and 35 MPa, respectively. The sample was consistently heated to the set temperature at a rate of 100 $^{\circ}\text{C min}^{-1}$. After sintering, it was cooled in the SPS chamber at an average cooling rate of 30 $^{\circ}\text{C min}^{-1}$ from the sintering temperature to room temperature. The axial load was removed simultaneously. A vacuum degree of 10 Pa in the SPS chamber was maintained throughout the heating/cooling process. Finally, the sample with a diameter of 30 mm and a thickness of 6 mm was obtained.

The microstructures and fracture surfaces of the composites were observed using an MR2000-type optical microscope and a SU8020-type field emission scanning electron microscope (SEM). Energy-dispersive spectroscopy (EDS) using an Oxford INCA instrument was conducted to analyze the micro-area composition. A thin plate of a thickness less than 50 μm was taken from the 5 wt.% GNF_A /6061Al matrix composite through high-speed wire electrical discharge machining. After grinding and polishing of the thin plate, a 3-mm-diameter disk was taken from the plate sample. Finally, the disk was recessed to about 10 μm in thickness and continuously reduced till perforation, using a Gatan-691-type ion thinner. A JEM-2100F-type field emission high-resolution transmission microscope (HRTEM) was then used to observe the interfacial morphologies of the composites. A LabRAM HR Evolution-type high-resolution Raman spectrometer was employed to analyze the carbon state of the GNFs. An X'Pert PRO MPD-type x-ray diffractometer (XRD) was used during phase analysis of the GNF/6061Al matrix composites with $\text{Cu K}\alpha$ radiation. The conditions were as follows: tube voltage, 20 kV; current, 200 mA; scanning rate, 3 $^{\circ}$ /min; and scanning range, 10 $^{\circ}$ –90 $^{\circ}$. The Archimedes' method was used to measure the densities of the GNF/6061Al matrix composites. The samples (50 mm \times 4 mm \times 3 mm) were used in the bending strength test in accordance with the Chinese national standard GB/T 6569-2006 (ISO 14704:2000) "Fine ceramics test method for flexural strength of monolithic ceramics at room temperature." The test was conducted using

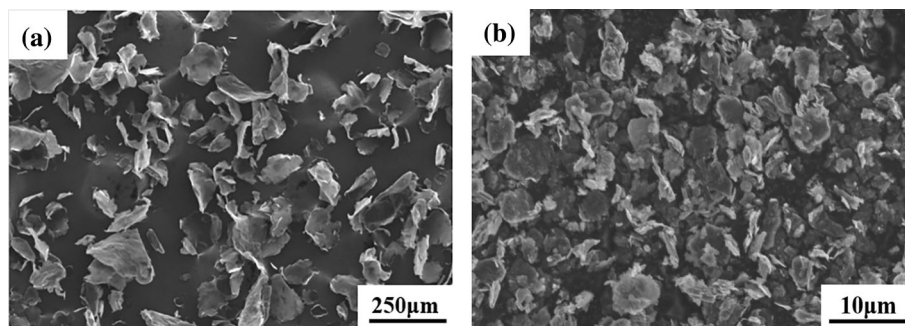


Fig. 1 SEM images showing the morphologies of (a) GNF_A and (b) GNF_B

an AG-X PLUS-type microcomputer control electronic universal testing machine with a testing span of 32 mm and a beam displacement rate of 0.5 mm min⁻¹. A LFA457-type laser thermal conductivity meter was used to measure the coefficient of thermal diffusion (α) of the composites using Ø6 mm × 3 mm disk-like samples. The TC of the composites was calculated as $TC = \alpha\rho c_p$, where α is the coefficient of thermal diffusivity (mm² s⁻¹), and ρ is the density (g cm⁻³) of the composites. c_p is the constant pressure heat capacity (J g⁻¹ K⁻¹) of the composites, which was calculated via the rule of mixtures (Ref 17), i.e., $c_p = c_m m_m + c_r m_r$, where c_m and c_r are the constant heat capacities of 6061 Al and GNFs, 0.896 and 0.71 J g⁻¹ K⁻¹, respectively. M_m and m_r refer to the mass fractions of 6061Al and GNFs of the composites, respectively, $m_m + m_r = 1$. Then, the c_p values of the 5, 10, and 15 wt.% GNF/6061 Al matrix composites were calculated as 0.886, 0.877, and 0.868 J g⁻¹ K⁻¹, respectively. The CTEs of the composite samples (10 mm × 5 mm × 3 mm) were tested using a TMA402F3-type thermal mechanical analyzer with a test temperature ranging from room temperature to 500 °C at a heating rate of 5 °C min⁻¹. The test was protected in a N₂ atmosphere at a flow rate of 20 mL min⁻¹.

3. Results and Discussion

3.1 Powder Characteristics

The 6061Al particles are mostly spherical and spheroidal (Fig. 2). After mechanical and ultrasonic stirring, the morphology of GNF_A in the GNF_A/6061Al powder mixture was unchanged. The GNF_A is randomly distributed in the 6061Al powder due to its larger size and smaller amount than the GNF_B (Fig. 2a). The GNF_B in the GNF_B/6061Al powder mixture has a smaller size than the 6061Al powder, where portions of it were fragmented and aggregated during the mixing process (Fig. 2b).

As shown in Fig. 3, two peaks at 1350 and 1580 cm⁻¹ in the Raman spectra are assigned to the characteristic D and G bands of the GNFs, respectively. The G band corresponds to the sp²-bonded graphitic carbon, while the D band is related to the structural defects including boundary vacancies, impurities, and voids (Ref 18, 19). The intensity ratio of the D band to the G band (I_D/I_G) can be employed to evaluate the defect densities of the GNFs. It is 0.2 (145.9/728.5) for the GNF_A and 0.23 (268.5/1138.4) for the GNF_B, respectively, meaning that the GNF_A has a higher degree of graphitization, and thus a higher thermal conductivity, compared with the GNF_B.

3.2 Microstructural Analyses

As shown in Fig. 4, the light gray zone is the 6061Al matrix and the black areas are GNFs. In the 10 wt.% GNF_A/6061Al matrix composites, most of the GNF_A is not in a distributed state (Fig. 4a). Since the 6061Al powder is approximately spherical, the GNF_A does not have specific orientation in the GNF_A/6061Al powder mixture. However, in the SPS process, the sample is greatly compressed in the axial direction under a large axial load (35 MPa). Significant displacement of the Al alloy particles and GNFs occurs in three dimensions, accompanying detectable plastic deformation of the 6061Al particles. It results in the deflection of the GNF_A, which is preferentially distributed in the X–Y direction. However, a portion of GNF_A has no apparent preferential orientation because it is curved and subjected to the extrusion of 6061Al particles shown in previous studies (Ref 20). Owing to the smaller size of GNF_B compared to GNF_A, the GNF_B in the 10 wt.% GNF_B/6061Al matrix composites is prone to agglomerate as it is much smaller than the 6061Al powder in size (Ref 21). However, the uniformity and dispersion of the GNF_B in the composite are promoted (Fig. 4b). The GNF_B distributes uniformly at the 6061Al grain boundaries, so the 6061Al matrix is severely separated. As a result, the atomic diffusion in the 6061Al matrix is dramatically inhibited in the SPS process of the composite. Thereby, the cross-sectional image of the 6061Al matrix is similar to the original 6061Al powder, as shown in Fig. 4(b). Full densification of the 6061Al matrix in the composite is challenging (Ref 22).

As shown in Fig. 5(a) and (c), the 6061Al matrix of the 10 wt.% GNF_A/6061Al composite is dense and shows a dimple aggregated ductile fracture mode. The GNF_A in the composite exists in two states: (1) The GNF_A lies on the fracture surface of the composite. As the composite fractures, the main fracture crack extends between the basal planes of the GNF_A. Two basal planes of the GNF_A are connected by π -bonding, which has an extremely low bonding strength (Ref 23). In the fracture of the composite, the fracture energy assimilated by the GNF_A is very low. (2) The basal plane of the GNF_A is perpendicular to the fracture surface of the composite, showing that the GNF_A particles were torn or pulled out in the X–Y direction in the fracture process of the composite. This phenomenon is due to σ -bonding in the basal plane of the GNF_A, which has a high bonding strength (Ref 23). Hence, tearing of the GNF_A consumes a large amount of energy, which greatly increases the main crack propagation resistance in the composite. Moreover, the difference of the plastic deformation ability of the GNF_A and that of the 6061Al matrix is so large that the GNF_A/6061Al interface of the composite is easily debonded

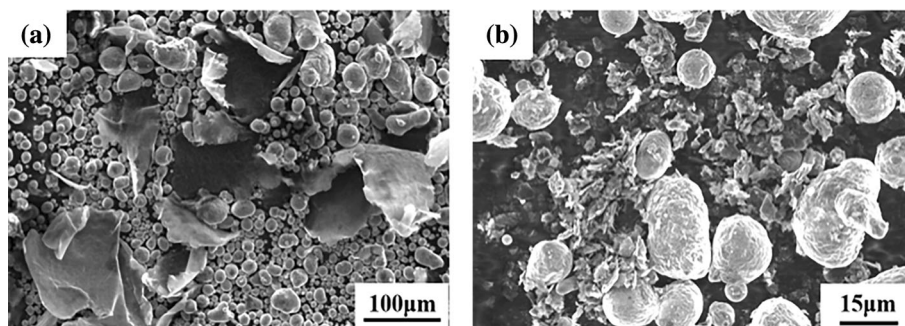


Fig. 2 SEM images of the morphologies of the 10 wt.% GNF/6061Al powder mixtures (a) GNF_A/6061Al and (b) GNF_B/6061Al

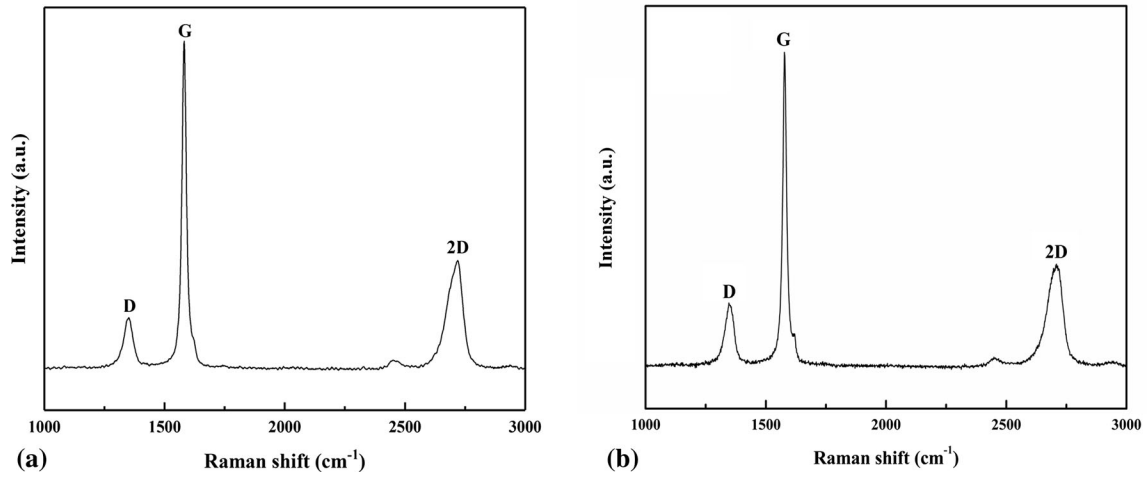


Fig. 3 Raman spectra of the GNFs (a) GNFA and (b) GNFB

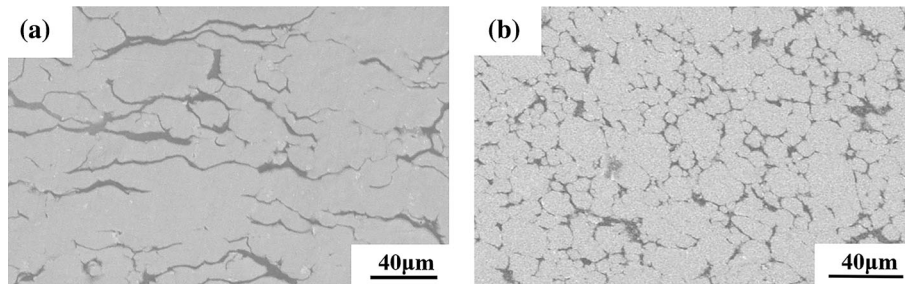


Fig. 4 Optical microscopy cross-sectional images of the 10 wt.% GNF/6061Al matrix composites (a) GNFA/6061Al and (b) GNFB/6061Al

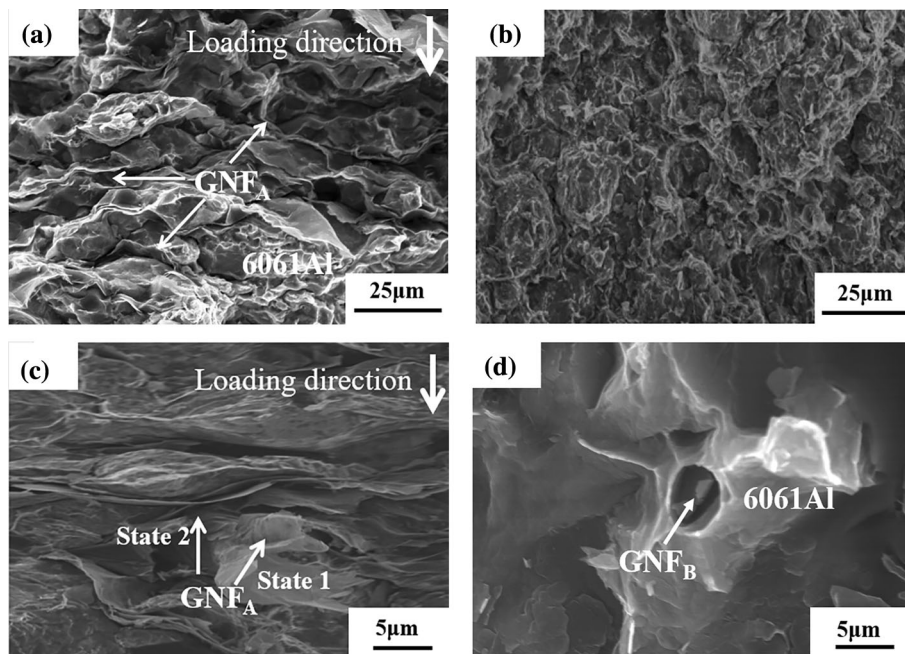


Fig. 5 SEM images showing bending fracture surfaces of the 10 wt.% GNF/6061Al matrix composites (a) GNFA/6061Al; (b) GNFB/6061Al; and (c, d) high-magnification images of (a) and (b), respectively

under an applied load (Ref 24), resulting in deep secondary cracks formed at the interface in the fracture process of the composite (Fig. 5c).

As mentioned above, the fine GNFB is semi-continuously distributed in the 10 wt.% GNFB/6061Al composite, which separates the 6061Al matrix and prohibits Al atomic diffusion.

Also, the density of the composite is low, as indicated by small spherical pores in the 6061Al matrix (Fig. 5d). As a result, brittle fracture of the 6061Al alloy matrix of the composite is dominant (Fig. 5b). Meanwhile, owing to the inhomogeneous deformation between the GNF_B and the Al alloy matrix, the GNF_B/6061Al interface is also debonded (Fig. 5d).

3.3 Interfacial Studies

As shown in Fig. 6(a), the GNF_A/6061Al interface in the 10 wt.% GNF_A/6061Al matrix composite is tight without any pores, and the interdiffusion of Al and C across the interface is not apparent in the SPS process. Similarly, in the 10 wt.% GNF_B/6061Al matrix composite, there is no obvious elemental interdiffusion at the GNF_B/6061Al interface. However, the interface is not close-knit, where couples of pores were found at the interface, as shown by the arrow in Fig. 6(b).

To specify the interfacial structure of the GNF/6061Al matrix composites and determine the presence of Al₄C₃ at the GNF/6061Al interface, the composites were further characterized by XRD and HRTEM, respectively. As shown in Fig. 7, only the graphite and Al diffraction peaks appear in the XRD patterns of the 10 wt.% GNF_A/6061Al and 10 wt.% GNF_B/6061Al matrix composites. Even the strongest diffraction peaks of Al₄C₃ (101), (012), and (107) planes, located at $2\theta = 30.5^\circ$ - 33.0° and 39.5° - 41.0° (Ref 25), are indiscernible in Fig. 7. It was concluded that no Al₄C₃ phase was formed, or the amount of the Al₄C₃ phase was so small that it could not be detected by XRD in the GNF/6061Al matrix composites fabricated in the low-temperature, rapid sintering process of SPS.

Using the 5 wt.% GNF_A/6061Al matrix composite as an example, the GNF/6061Al interfacial structure was clarified by HRTEM (Fig. 8). An irregular black line in Fig. 8(a) refers to a 6061Al grain boundary, which is composed of high-density dislocations (Ref 26). In Fig. 8(a), the GNF_A/6061Al interfacial

zone can be clearly identified. The GNF_A contacts with the 6061Al matrix tightly, where no interfacial pores or needle-like Al₄C₃ reaction products were observed (Ref 27). Figure 8(b) further confirms an interfacial transition zone 15-18 nm thick existed at the GNF_A/6061Al interface. The atomic planes of the interfacial transition zone are indistinguishable. The selected area electron diffraction (SAED) spectrum of the GNF_A/6061Al interface zone is shown in Fig. 8(c). There are two different diffraction patterns in the spectrum, i.e., the central diffuse ring of graphite and the diffraction spots of Al. It provides evidence of an amorphous phase in the interfacial zone. According to Ref 25 and 28, the interfacial transition zone may consist of two

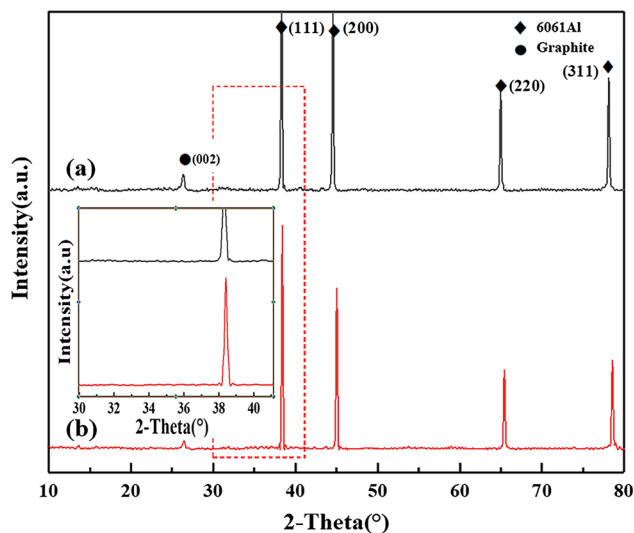


Fig. 7 XRD patterns of the 10 wt.% GNF/6061Al matrix composites (a) GNF_A/6061Al and (b) GNF_B/6061Al

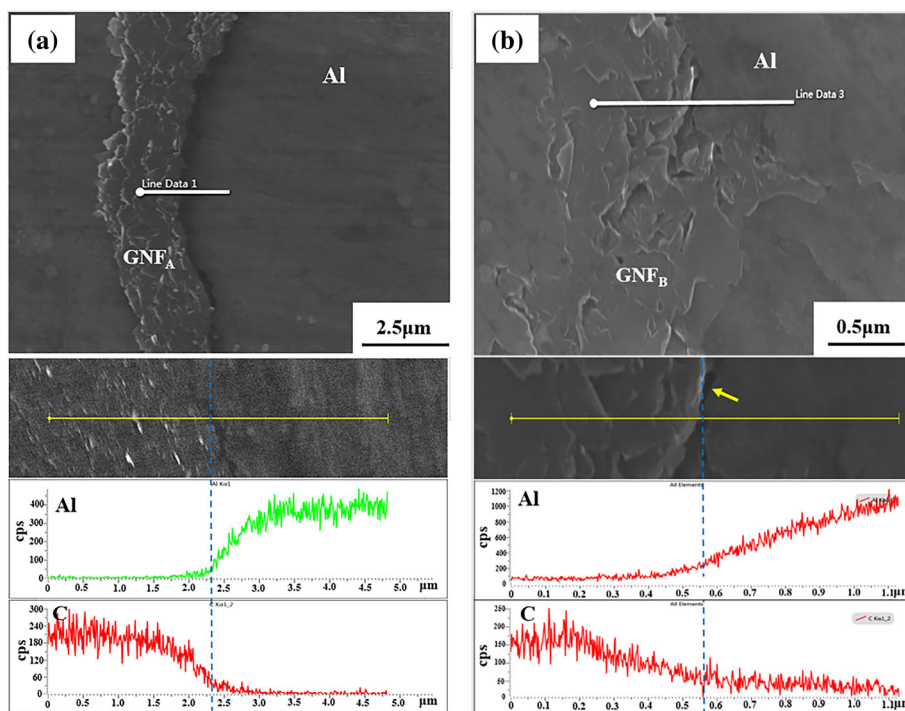


Fig. 6 SEM images and EDS elemental linear scanning curves across the GNF/6061Al interfaces of the 10 wt.% GNF/6061Al matrix composites (a) GNF_A/6061Al and (b) GNF_B/6061Al

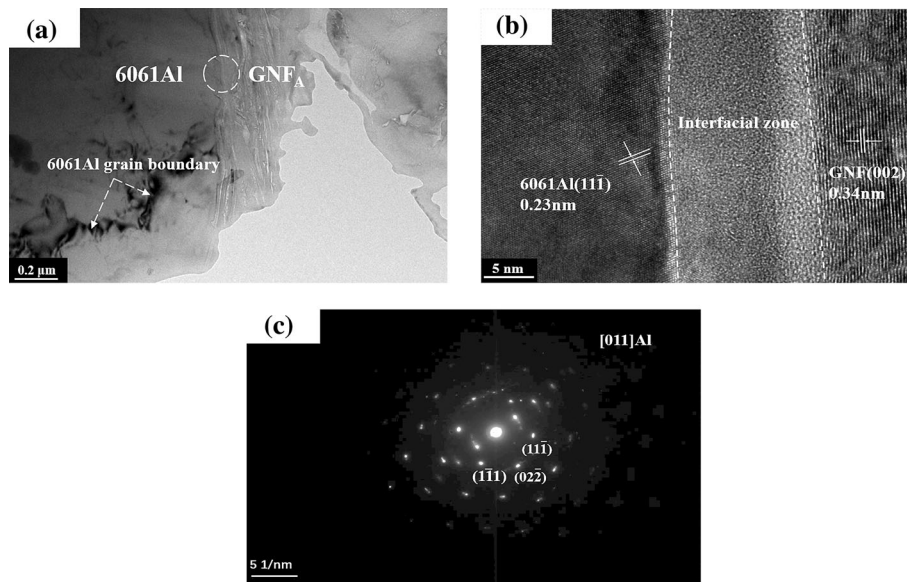


Fig. 8 (HR)TEM images and SAED patterns of the 5 wt.% GNF_A/6061Al matrix composite (a) TEM bright-field image; (b) HRTEM image of the circular area in (a); and (c) SAED spectrum of the interfacial zone

layers, i.e., a poorly crystalline layer close to the 6061Al matrix and an amorphous layer adjacent to the GNF_A. By means of the interfacial transition zone, the GNF_A is closely contacted with the 6061Al matrix. In contrast, due to the presence of the amorphous layer, the interfacial thermal resistance of the composites increases, which has a negative effect on the TCs of the GNF/6061Al matrix composites.

The Al₄C₃ phase is primarily generated at the carbon/Al interface at conditions of high sintering temperature and long duration at high temperature (Ref 29). If the sintering temperature and holding time of the composites are decreased, the formation of the Al₄C₃ phase can be effectively inhibited or even prevented (Ref 30, 31). In this work, the SPS technique was employed to fabricate GNF/6061Al matrix composites at low temperature of 610 °C for a short holding time of 10 min. The heating/cooling rates were relatively high, 100 and 30 °C min⁻¹, respectively. The sintering temperature was about 30 °C lower, and the holding time was 50 min shorter than those of the graphite/Al matrix composites fabricated via hot pressing (Ref 32). One of the benefits of the SPS process for GNF/6061Al matrix composites is that the formation of the Al₄C₃ phase is inhibited. Similarly, with the low-temperature, rapid sintering of the SPS technology, the interfacial transition zone of the 5 wt.% GNF_A/6061Al matrix composites is thinner than that of the graphite/Al matrix composites (40-50 nm in thickness) fabricated by the infiltration method (Ref 25).

In summary, the microstructures and interfacial structures of GNF/6061Al matrix composites are significantly improved via the SPS technique. Comparatively, the GNF_A/6061Al matrix composites have better microstructures than the GNF_B/6061Al matrix composites, as shown in Fig. 4-6.

3.4 Relative Density and Bending Strength

The relative densities of the two GNF/6061Al matrix composites are lower than that of the as-sintered 6061Al (99.1%) and continuously decrease with increasing GNF fraction from 5 to 15 wt.%; however, they are always greater than 97% (Fig. 9). In contrast, the relative density of the 5 wt.% GNF/Al composite fabricated via pressureless sintering

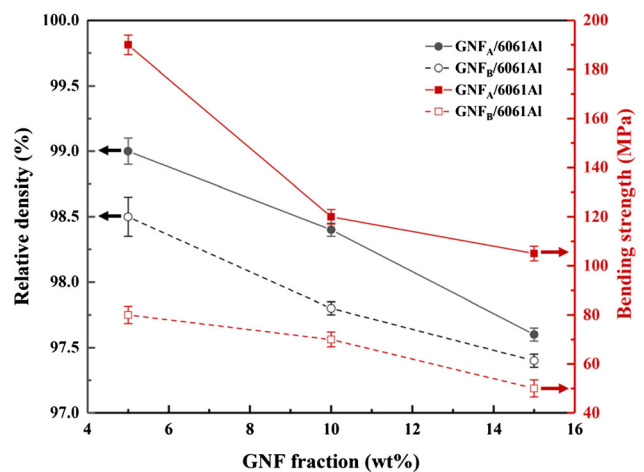


Fig. 9 Plots of relative densities and bending strengths of the GNF/6061Al matrix composites vs. GNF fraction

is only about 73% (Ref 9). Therefore, the SPS technique is shown to be very effective in achieving rapid densification of the GNF/Al matrix composites. In addition, the relative densities of the GNF_A/6061Al matrix composites are higher than those of the GNF_B/6061Al matrix composites at the same GNF fraction. This result is consistent with the microstructures of the composites shown in Fig. 4-6. Similarly, the bending strengths of the GNF/6061Al matrix composites are also lower than that of the as-sintered 6061Al (310 MPa) and steadily decrease with increasing GNF fraction. Meanwhile, the GNF_A/6061Al matrix composites show higher bending strengths than the GNF_B/6061Al composites of the same GNF fraction (Fig. 9 and 10), which is related to higher relative densities and better microstructures of the former. It is worth noting that even though the GNF fraction is as high as 15 wt.%, the GNF_A/6061Al matrix composites show a bending strength greater than 100 MPa, which is much stronger than the 15 wt.% graphite flakes/2014Al composite fabricated using the in situ powder metallurgy technique (23 MPa) (Ref 33). Moreover, at least

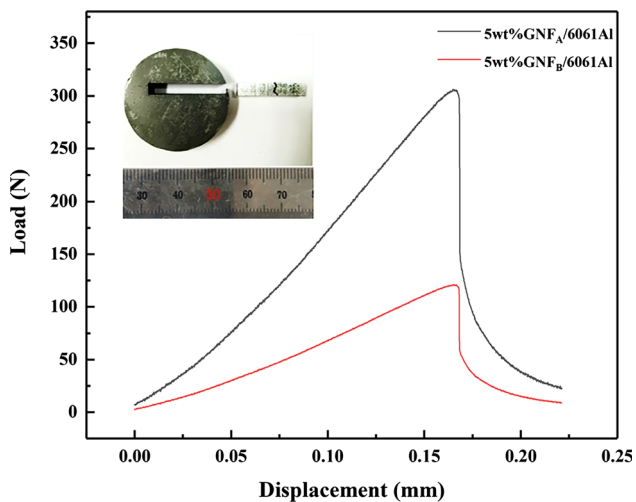


Fig. 10 Load–displacement curves of 5 wt.% GNF/6061Al matrix composites via three-point bending tests

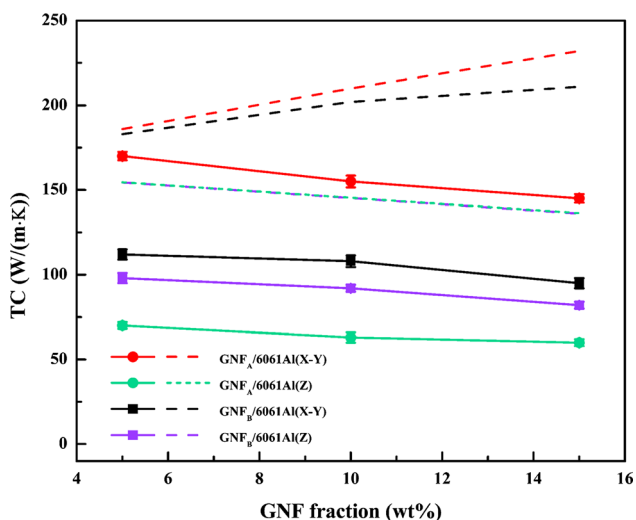


Fig. 11 Tested (solid lines) and model predicted (dotted lines) TCs of GNF/6061Al matrix composites with respect to GNF fraction

30 MPa bending strength is required for undamaged packaging of semiconductor components and devices during installation and transport (Ref 34). The bending strengths of all GNF/6061Al matrix composites developed in this study meet this standard.

3.5 Thermal Conductivity

The TCs of the GNF/6061Al matrix composites in the X – Y and Z directions decrease monotonically with increasing GNF fraction (Fig. 11), and most of them are less than that of the as-sintered 6061Al alloy ($163.6 \text{ W m}^{-1} \text{ K}^{-1}$), primarily due to poor microstructures and interfacial states of the composites with higher GNF fraction. The TCs of the 5 wt.% GNF_A/6061Al matrix composite in the X – Y and Z directions are 170 and $70 \text{ W m}^{-1} \text{ K}^{-1}$, respectively. There is a difference of about $100 \text{ W m}^{-1} \text{ K}^{-1}$, the largest one of all GNF/6061Al matrix composites in this study (Fig. 11). As reported by Oddone et al., the 50 vol.% (40 wt.%) graphite flakes ($500 \mu\text{m} \times 10 \mu\text{m}$ in size)/Al matrix composite showed a TC up to

$370 \text{ W m}^{-1} \text{ K}^{-1}$ in the X – Y direction, but a TC as low as $40 \text{ W m}^{-1} \text{ K}^{-1}$ in the Z direction. The difference is more than $300 \text{ W m}^{-1} \text{ K}^{-1}$, indicating remarkable anisotropy of the composite (Ref 5). With respect to TC, the anisotropies of the GNF/6061Al matrix composites are significantly reduced by choosing smaller-sized GNFs. As shown in Fig. 11, the GNF_B/6061Al matrix composites have higher TCs in the Z direction than the GNF_A/6061Al matrix composites of the same GNF fraction, although the TCs in the X – Y direction of the former are lower. The TC difference is as low as $15 \text{ W m}^{-1} \text{ K}^{-1}$ in the 15 wt.% GNF_B/6061Al matrix composite, the smallest one of all GNF/6061Al matrix composites (Fig. 11). The significant reduction in anisotropy of the GNF_B/6061Al matrix composites is attributed to the low distribution orientation of the GNF_B in the composites. It was concluded that a reduction in GNFs size resulted in a reduction in the TC difference in the X – Y and Z directions of the GNF/6061Al matrix composites, generating composites with high TCs in three dimensions.

The TCs of the GNF/6061Al matrix composites can be predicted via a modified Maxwell model (Ref 35):

$$K_c = K_m \frac{K_r + (n-1)K_m + (n-1)V(K_r - K_m)}{K_r + (n-1)K_m - V(K_r - K_m)} \quad (\text{Eq 1})$$

where K_c , K_m , and K_r are the TCs of the composites, the 6061Al matrix ($163.6 \text{ W m}^{-1} \text{ K}^{-1}$), and the GNF_A and GNF_B (600 and $500 \text{ W m}^{-1} \text{ K}^{-1}$ in the X – Y direction estimated by the XRD results in Fig. 7 in accordance with Ref 36 and 37 and $15 \text{ W m}^{-1} \text{ K}^{-1}$ in the Z direction (Ref 38), respectively. V is the volume fraction of the reinforcements, and n is the shape factor of the reinforcements, where $n = 3/\psi$, and ψ is the degree of sphericity of the reinforcements. Regarding the GNFs as cylinders of a very small thickness, the degree of sphericity

of the GNFs, $\psi = \frac{3\sqrt{\frac{9RH^2}{2}}}{R+H}$, where R and H are the average radius and thickness of the GNFs, they are 30 and $0.1 \mu\text{m}$ for GNF_A, and 2.5 and $0.02 \mu\text{m}$ for GNF_B, respectively. So, the ψ values of GNF_A and GNF_B were calculated as 27.23 and 45.46, respectively, and thus, the n values of GNF_A and GNF_B were obtained. Finally, the relationships between K_c of the GNF/6061Al matrix composites and the GNF fraction were deduced in accordance with Eq 1, as shown in Fig. 11. The TCs of the GNF/6061Al matrix composites are always less than the model predicted values, and the discrepancies increase as the GNF fraction of the composite increases. The thermal resistance increment results from the nonideal microstructures of the composites, such as pores, aggregation of the GNFs, and the GNF/6061 interfaces.

3.6 Coefficient of Thermal Expansion

As shown in Fig. 12, the CTE values (RT–100 °C) of two GNF/6061Al matrix composites decrease monotonically as the GNF fraction increases from 5 to 15 wt.% and always lower than that of the as-sintered 6061Al alloy (19 ppm K^{-1}). Generally, the CTEs of composites depend on the characteristics and contents of the phase components, the density, interfacial state, and the residual stress inside the composite (Ref 17). Overall, interfacial bonding is the key factor affecting the thermal expansion properties of the GNF/6061Al composites. The interfacial bonding between the GNF_A and the 6061Al matrix is higher than that between the GNF_B and the 6061Al matrix, so the GNF_A has a higher inhibitory effect on the

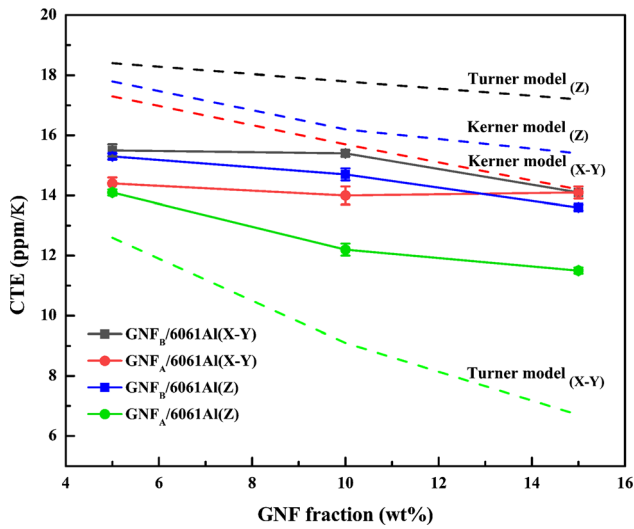


Fig. 12 Tested (solid lines) and model predicted (dotted lines) CTEs of GNF/6061Al matrix composites vs. GNF fraction

Table 1 Physical properties of 6061Al and GNFs employed in CTE calculations via the Kerner and Turner models (Ref 41, 44, 45)

	α , ppm K ⁻¹	E , GPa	ν	K , GPa	G , GPa
6061Al	19 (this work)	70	0.33	68.55	26.6
GNFs (X - Y)	-1	1020	0.16	500	440
GNFs (Z)	-26	38.5	0.012	13.1	19

thermal expansion of the 6061Al matrix than the GNF_B (Ref 39). As a result, the CTEs of the GNF_A/6061Al matrix composites in both the X - Y direction and the Z direction are lower than those of the GNF_B/6061Al matrix composites of the same GNF fraction.

Since the CTE of the graphite flake in the X - Y direction (-1 ppm K⁻¹) is much less than that in the Z direction (28 ppm K⁻¹) (Ref 40), it is assumed that the CTEs of the GNF/6061Al matrix composites in the Z direction will be significantly higher than those of the composites in the X - Y direction. However, the experimental result in this work shows an opposing trend. The CTEs of the GNF/6061Al matrix composites in the Z direction are lower than those of the composites in the X - Y direction. Similar phenomena were found in the graphite flakes reinforced 7075 Al, Mg-0.9 Ca, and Cu matrix composites prepared by SPS (Ref 5, 40). Firkowska et al. (Ref 41) have developed a model concerning the mechanical and thermal interactions between the graphite flakes and metal matrix based on elastic theory and the sandwich structure characteristics of the composites. In the 50 vol.% graphite flakes/Cu matrix composite, the CTE of the graphite flakes in the Z direction predicted by the model is -26 ppm K⁻¹, which is much lower than that of the graphite flakes in the X - Y direction. It also presents a satisfactory explanation for the experimental results in Fig. 12.

Generally, the Turner model is used to predict the CTE of composites undergoing uniform hydrostatic stress (Ref 42):

$$\alpha_c = \frac{\alpha_m(1-V)K_m + \alpha_r VK_r}{(1-V)K_m + VK_r} \quad (\text{Eq 2})$$

where α and V are the CTE and the volume fraction of the reinforcements. K is the bulk modulus, $K = \frac{E}{3(1-2\nu)}$, where E and ν are the Young's modulus and the Poisson ratio. The subscripts c , m , and p are the composites, the 6061Al matrix, and the reinforcements, respectively.

In the Kerner model, both the normal and shear stresses are taken into account (Ref 43):

$$\alpha_c = \alpha_m(1-V) + \alpha_r V + (1-V)V(\alpha_r - \alpha_m) \times \frac{K_r - K_m}{(1-V)K_m + VK_r + 3(K_m K_r / 4G_m)} \quad (\text{Eq 3})$$

where G is the shear modulus, $G = \frac{E}{2(1+\nu)}$. The values of the parameters used above for the Turner and Kerner model calculations are listed in Table 1.

Accordingly, the relationships between the CTEs of the GNF/6061Al matrix composites and the GNF fraction were deduced in accordance with Eq 2 and 3, as shown in Fig. 12. The CTEs of the GNF/6061Al matrix composites are closer to the results predicted by the Kerner model, but in a low level in both X - Y and Z directions. It is primarily because the flake graphite particles, instead of the spherical ones, are used as the reinforcements in the composites, which exert a more intensive restraining effect on the thermal expansion of the composites than the spherical ones (Ref 46). Moreover, the pores in the GNF/6061Al matrix composites also play a role in restraining the thermal expansion of the composites.

Compared with other graphite flakes/Al matrix composites of comparable graphitic flake fractions, the 5 wt.% (6 vol.%) GNF/6061Al matrix composites in this work have lower CTEs in both the X - Y and Z directions (Table 1). In Ref 31 and 33, the large natural graphite flakes were employed to produce the graphite flakes/Al matrix composites, where the inhibitory effect of GNFs on the thermal expansion of the Al matrix in three dimensions is lessened. In this study, the GNF/6061Al matrix composites were developed using small and thin GNFs. The CTEs of these composites are significantly less, attributable to the excellent microstructures and interfacial bonding states of the composites (Table 2).

4. Conclusions

- (1) In terms of ultrasonic and mechanical stirring, uniform dispersion and mixing of GNFs in 6061Al powder were achieved. After SPS at 610 °C for 10 min at a load of 35 MPa, the GNF_A/6061Al matrix composites were dense. The GNF_A in the composites is preferentially distributed in the X - Y direction. However, the GNF_B in the GNF_B/6061Al matrix composites tends to isotropically distribute. The GNF_B is distributed uniformly along the 6061Al grain boundaries, which strongly discourages sintering densification of the GNF_B/6061Al matrix composites.
- (2) In the GNF_A/6061Al matrix composites, the GNF_A shows strong bonding with the 6061Al alloy matrix. Under an applied load, the fracture of the Al alloy is a dimple aggregation ductile fracture mode, where the gra-

Table 2 Comparison of the CTEs of several graphite flakes/Al matrix composites

Graphite flake fraction, vol.%	Sintering process	CTE, ppm K ⁻¹		Refs.
		X–Y	Z	
10	HP, 640 °C, 60 MPa	17.1	15.3	31
10	HP, 600 °C, 60 MPa	24.2	...	33
6 (GNF _A)	SPS, 610 °C, 35 MPa	14.4	14.1	This work
6 (GNF _B)	SPS, 610 °C, 35 MPa	15.5	15.3	This work

phite flakes are torn and/or pulled out from the Al alloy matrix. In the GNF_B/6061Al matrix composites, the 6061Al matrix is not dense, and the GNF_B/6061Al interfacial bonding is weak. Under an applied load, the fracture of the Al alloy is in brittle fracture mode, accompanied by debonding of the GNF_B from the 6061Al matrix.

- (3) 15-18-nm-thickness interfacial transition zones exist in the 5 wt.% GNF_A/6061Al matrix composites, which are composed of a poorly crystalline layer close to the 6061Al matrix and an amorphous layer adjacent to the GNF_A. No Al₄C₃ is generated in the transition zone. In terms of the interfacial transition zone, strong interfacial bonding was generated between the GNF_A and the 6061Al matrix.
4. The relative densities, bending strengths, TCs, and CTEs of two types of the GNF/6061Al matrix composites decrease with increasing GNF fraction. The GNF_A/6061Al matrix composites show higher densities, strengths, and TCs in the X–Y direction, and lower CTEs compared to the GNF_B/6061Al matrix composites. In contrast, the GNF_B/6061Al matrix composites show higher TCs in the Z direction and lower TC and CTE differences in the X–Y and Z directions. The anisotropy of the microstructures and properties of the GNF/6061Al (GNF_A or GNF_B) matrix composites in three dimensions are significantly reduced by decreasing the GNF size.

Acknowledgments

This work was financially supported by International Science & Technology Cooperation Program of China (Grant Numbers 2014DFA50860).

References

1. G. Yuan, X. Li, Z. Dong, A. Westwood, Z.W. Cui, Y. Cong, H.D. Du, and F.Y. Kang, Graphite Blocks with Preferred Orientation and High Thermal Conductivity, *Carbon*, 2012, **50**, p 175–182
2. C. Zweben, Ultrahigh-Thermal-Conductivity Packaging Materials, in *IEEE: Twenty First Annual IEEE Semiconductor Thermal Measurement and Management Symposium*, March 15–17, 2005 (IEEE, San Jose, CA, USA, 2005)
3. S.S. Sidhu, S. Kumar, and A. Batish, Metal Matrix Composites for Thermal Management: A Review, *Crit. Rev. Solid State Mater. Sci.*, 2016, **41**, p 132–157
4. J.D. Mathias, P.M. Geffroy, and J.F. Silvain, Architectural Optimization for Microelectronic Packaging, *Appl. Therm. Eng.*, 2009, **29**, p 2391–2395

5. V. Oddone, B. Boerner, and R. Reich, Composites of Aluminum Alloy and Magnesium Alloy with Graphite Showing Low Thermal Expansion and High Specific Thermal Conductivity, *Sci. Technol. Adv. Mater.*, 2017, **8**, p 180–186
6. H. Kwon, M. Estili, K. Takagi, T. Miyazaki, and A. Kawasaki, Combination of Hot Extrusion and Spark Plasma Sintering for Producing Carbon Nanotube Reinforced Aluminum Matrix Composites, *Carbon*, 2008, **47**, p 570–577
7. M. Rashad, F. Pan, A. Tang, and M. Asif, Effect of Graphene Nanoplatelets Addition on Mechanical Properties of Pure Aluminum Using a Semi-powder Method, *Prog. Nat. Sci.*, 2014, **24**, p 101–108
8. A.A. Balandin, S. Ghosh, W. Bao, I. Calizo, D. Teweldebrhan, F. Miao, and C.N. Lau, Superior Thermal Conductivity of Single-Layer Graphene, *Nano Lett.*, 2008, **8**, p 902–907
9. S.N. Alam and L. Kumar, Mechanical Properties of Aluminum-Based Metal Matrix Composites Reinforced with Graphite Nanoplatelets, *Mater. Sci. Eng. A*, 2016, **667**, p 16–32
10. T.T. Liu, X.B. He, L. Zhang, Q. Liu, and X.H. Qu, Fabrication and Thermal Conductivity of Short Graphite Fiber/Al Composites by Vacuum Pressure Infiltration, *J. Compos. Mater.*, 2014, **48**, p 2207–2214
11. A. Saboori, M. Pavese, and C. Badini, Development of Al- and Cu-Based Nanocomposites Reinforced by Graphene Nanoplatelets: Fabrication and Characterization, *Front. Mater. Sci.*, 2017, **11**, p 171–181
12. X. Gao, H. Yue, E. Guo, H. Zhang, X.Y. Lin, L.H. Yao, and B. Wang, Mechanical Properties and Thermal Conductivity of Graphene Reinforced Copper Matrix Composites, *Powder Technol.*, 2016, **301**, p 601–607
13. A. Boden, B. Boerner, P. Kusch, I. Firkowska, and S. Reich, Nanoplatelet Size to Control the Alignment and Thermal Conductivity in Copper-Graphite Composites, *Nano Lett.*, 2014, **14**, p 3640–3644
14. G. Li and B. Xiong, Effects of Graphene Content on Microstructures and Tensile Property of Graphene-Nanosheets/Aluminum Composites, *J. Alloys Compd.*, 2017, **697**, p 31–36
15. M. Tokita, Trends in Advanced SPS Spark Plasma Sintering Systems and Technology, *J. Soc. Powder Technol. Jpn.*, 1993, **30**, p 790–804
16. K. Mizuuchi, K. Inoue, Y. Agari, T. Nagaoka, M. Sugioka, M. Tanaka, T. Takeuchi, J. Tani, M. Kawahara, Y. Makino, and M. Ito, Processing of Al/SiC Composites in Continuous Solid–Liquid Co-existent State by SPS and Their Thermal Properties, *Compos. B*, 2012, **4**, p 2012–2019
17. X.Z. Mao, Y.Q. Huang, and B.H. Wang, Fabrication, Microstructures and Properties of 50 vol.%SiCp/6061Al Composites via a Pressureless Sintering Technique, *Powder Metall.*, 2017, **61**, p 1–9
18. A. Nieto, A. Bisht, D. Lahiri, C. Zhang, and A. Agarwal, Graphene Reinforced Metal and Ceramic Matrix Composites: A Review, *Int. Mater. Rev.*, 2016, **62**, p 241–302
19. A.C. Ferrari, J.C. Meyer, V. Scardaci, C. Casiraghi, M. Lazzeri, F. Mauri, S. Piscanec, D. Jiang, K.S. Novoselov, S. Roth, and A.K. Geim, Raman Spectrum of Graphene and Graphene Layers, *Phys. Rev. Lett.*, 2016, **97**, p 187401
20. C. Nabil, M. Diaa, D. Florence, C. Nathalie, Y.F. Lu, and J.F. Silvain, Effect of Flake Powder Metallurgy on Thermal Conductivity of Graphite Flakes Reinforced Aluminum Matrix Composites, *J. Mater. Sci.*, 2018, **53**, p 8180–8192
21. T. Varol and A. Canakci, Microstructure, Electrical Conductivity and Hardness of Multilayer Graphene/Copper Nanocomposites Synthesized by Flake Powder Metallurgy, *Met. Mater. Int.*, 2015, **21**, p 704–712
22. A. Saboori, M. Pavese, and C. Badini, Microstructure and Thermal Conductivity of Al-Graphene Composites Fabricated by Powder

- Metallurgy and Hot Rolling Techniques, *Acta Metall. Sin.*, 2017, **30**, p 675–687
23. D. Lin, L.C. Richard, and G.J. Cheng, Single-Layer Graphene Oxide Reinforced Metal Matrix Composites by Laser Sintering: Microstructure and Mechanical Property Enhancement, *Acta Mater.*, 2014, **80**, p 183–193
 24. K. Bo, T.X. Fan, and J.M. Ru, Improved Wetting and Thermal Properties of Graphite-Cu Composite by Cr-Solution Immersion Method, *Diam. Relat. Mater.*, 2016, **65**, p 191–197
 25. C. Zhou, G. Ji, Z. Chen, M.L. Wang, A. Addad, D. Schryvers, and H.W. Wang, Fabrication, Interface Characterization and Modeling of Oriented Graphite Flakes/Si/Al Composites for Thermal Management Applications, *Mater. Des.*, 2014, **63**, p 719–728
 26. M.P. Liu, T.H. Jiang, X.F. Xie, Q. Liu, X.F. Li, and J.R. Hans, Microstructure Evolution and Dislocation Configurations in Nanostructured Al-Mg Alloys Processed by High Pressure Torsion, *Trans. Nonferr. Met. Soc. China*, 2014, **24**, p 3848–3857
 27. H. Kwon, M. Estili, K. Takagi, T. Miyazaki, and A. Kawasaki, Combination of Hot Extrusion and Spark Plasma Sintering for Producing Carbon Nanotube Reinforced Aluminum Matrix Composites, *Carbon*, 2009, **47**, p 570–577
 28. W. Li, Y. Liu, and G. Wu, Preparation of Graphite Flakes/Al with Preferred Orientation and High Thermal Conductivity by Squeeze Casting, *Carbon*, 2015, **95**, p 545–551
 29. T. Etter, P. Schulz, M. Weber, J. Metz, M. Wimpler, J.F. Löffler, and P.J. Uggowitzer, Aluminium Carbide Formation in Interpenetrating Graphite/Aluminium Composites, *Mater. Sci. Eng. A*, 2007, **448**, p 1–6
 30. T. Etter, J. Kuebler, T. Frey, P. Schulz, J.F. Löffler, and P.J. Uggowitzer, Strength and Fracture Toughness of Interpenetrating Graphite/Aluminium Composites Produced by the Indirect Squeeze Casting Process, *Mater. Sci. Eng. A*, 2004, **386**, p 61–67
 31. J. Leng, G. Wu, Q. Zhou, Z.Y. Dou, and X.L. Huang, Mechanical Properties of SiC/Gr/Al Composites Fabricated by Squeeze Casting Technology, *Scr. Mater.*, 2008, **59**, p 619–622
 32. J.K. Chen and I.S. Huang, Thermal Properties of Aluminum-Graphite Composites by Powder Metallurgy, *Compos. B*, 2013, **44**, p 698–703
 33. F. Akhlaghi and A. Zare-Bidaki, Influence of Graphite Content on the Dry Sliding and Oil Impregnated Sliding Wear Behavior of Al2024/Graphite Composites Produced by In Situ Powder Metallurgy Method, *Wear*, 2009, **266**, p 37–45
 34. Y. Xu, Research on Preparation and Properties of Graphite/Copper Composites with High Thermal Conductivity, Master Thesis, Huazhong University of Science and Technology, China, vol 1 (2013), p. 33. (In Chinese)
 35. J.Z. Xu, B.Z. Gao, and F.Y. Kang, A Reconstruction of Maxwell Model for Effective Thermal Conductivity of Composite Materials, *Appl. Therm. Eng.*, 2016, **102**, p 972–979
 36. M. Xiao, X.W. Zhang, W.T. Xiao, J.J. Du, H.H. Song, and Z.K. Ma, The Influence of Chemical Constitution on the Structure and Properties of Polyimide Fibre and Their Graphite Fibre, *Polymer*, 2019, **165**, p 142–151
 37. P.M. Adams, H.A. Katzman, G.S. Rellick, and G.W. Stupian, Characterization of High Thermal Conductivity Carbon Fibers and a Self-reinforced Graphite Panel, *Carbon*, 1998, **36**, p 233–245
 38. L. Wei, R. Zhang, and C.P. Wong, Modeling of Thermal Conductivity of Graphite Nanosheet Composites, *J. Electron. Mater.*, 2010, **39**, p 268–272
 39. K. Hiroki, M. Takamichi, K. Akira, Y.F. Lu, and J.F. Silvain, Interfacial Microstructure of Graphite Flake Reinforced Aluminum Matrix Composites Fabricated via Hot Pressing, *Compos. A*, 2015, **73**, p 125–131
 40. J.B. Nelson and D.P. Riley, The Thermal Expansion of Graphite from 15 to 800 °C: Part I. Experimental, *Proc. Phys. Soc.*, 1945, **57**, p 477
 41. I. Firkowska, A. Boden, B. Boerner, and S. Reich, The Origin of High Thermal Conductivity and Ultralow Thermal Expansion in Copper-Graphite Composites, *Nano Lett.*, 2015, **15**, p 4745–4751
 42. P.S. Turner, Thermal-Expansion Stresses in Reinforced Plastics, *J. Res. Natl. Bur. Stand.*, 1946, **37**, p 239–250
 43. E.H. Kerner, The Elastic and Thermo-Elastic Properties of Composite Media, *Proc. Phys. Soc. B*, 1956, **69**, p 808–813
 44. X.M. Zhu, J.K. Yu, and X.Y. Wang, Microstructure and Properties of Al/Si/SiC Composites for Electronic Packaging, *Trans. Nonferr. Met. Soc.*, 2012, **22**, p 1686–1692
 45. O.L. Blakslee, D.G. Proctor, E.J. Seldin, G.B. Spence, and T. Weng, Elastic Constants of Compression-Annealed Pyrolytic Graphite, *J. Appl. Phys.*, 1970, **41**, p 3373–3382
 46. J. Sun, G.H. Chen, B.H. Wang, G.D. Chen, and W.M. Tang, Fabrication, Microstructures, and Properties of 50 vol.% SiCp/6061Al Composites via Hot Pressing, *J. Mater. Eng. Perform.*, 2019, **28**, p 2697–2706

Publisher's Note Springer Nature remains neutral with regard to jurisdictional claims in published maps and institutional affiliations.